Applied Catalysis B: Environmental 335 (2023) 122893

Contents lists available at ScienceDirect

Applied Catalysis B: Environmental

journal homepage: www.elsevier.com/locate/apcatb

Selective hydrogenolysis of 5-hydroxymethylfurfural to 5-methylfurfural over Au/TiO_2

Lin Dong [a], Jordi Morales-Vidal [b,c], Lili Mu [a], Licheng Li [a], Núria López [b], Javier Pérez-Ramírez [d], Zupeng Chen [a,*]

[a] Jiangsu Co-Innovation Center of Efficient Processing and Utilization of Forest Resources, International Innovation Center for Forest Chemicals and Materials, College of Chemical Engineering, Nanjing Forestry University, Longpan Road 159, Nanjing 210037, China
[b] Institute of Chemical Research of Catalonia (ICIQ-CERCA), The Barcelona Institute of Science and Technology, Av. Països Catalans 16, 43007 Tarragona, Spain
[c] Universitat Rovira i Virgili, Av. Catalunya 35, 43002 Tarragona, Spain
[d] Institute for Chemical and Bioengineering, Department of Chemistry and Applied Biosciences, ETH Zürich, Vladimir-Prelog-Weg 1, 8093 Zürich, Switzerland

ARTICLE INFO

Keywords:
5-hydroxymethylfurfural
Selective hydrogenolysis
5-methylfurfural
Gold-based catalyst
Biomass valorization

ABSTRACT

5-Methylfurfural (MF) is a critical commodity chemical used as food additive and synthetic intermediate. Opening a sustainable route towards highly selective synthesis of MF from 5-hydroxymethylfurfural (HMF) is of great significance, but has demonstrated extremely challenging. Herein, we report an efficient process for the selective production of MF from HMF over an anatase-supported gold catalyst (Au/a-TiO_2). During the hydrogenolysis of HMF, the desired C═O bond is maintained and MF can be obtained in a high yield of 83.1 %, exhibiting excellent stability both in batch and flow operation. A combination of experimental and theoretical analyses attribute the superior performance of Au/a-TiO_2 to the synergistic effect of limited H access, low adsorption of reactants, and avoiding condensation, driven by the high concentration of oxygen vacancies in the support. This study highlights a novel approach of tailoring the coverage of active species for the selective transformation of renewable compounds into high-value-added chemicals.

1. Introduction

Biomass is widely recognized as the only renewable organic carbon resource on Earth and its conversion to value-added chemicals and fuel has the potential of being the substitute for traditional petrochemicals [1–4]. 5-hydroxymethylfurfural, HMF, can be obtained from cellulose and it is an important biomass-derived platform compound for the production of a wide spectrum of sustainable bioproducts, biofuels, and polyesters [5–9]. Particularly, the selective hydrogenolysis of HMF to different high-value chemicals has attracted much interest in sustainable biorefinery [10–12]. The coexistence of three kinds of O-related functional groups in HMF (i.e., hydroxyl group, aldehyde group, and furan ring) imposes challenges for the selective synthesis of dimethylfuran (DMF) [13–15], 2,5-furandimethanol (FDM) [16], 2,5-di-hydroxy-methyl-tetrahydrofuran (DHMTHF) [17], 2-hexanol [18], and 5-methylfurfural (MF) [19,20].

Among these products, MF is one of the most important furan chemicals, which can be utilized as food additive, intermediate in the production of agrochemicals, and precursor of certain anti-cancer natural products [21–24]. Thus, the selective conversion of HMF into MF is of critical importance, despite the challenges associated with the different functional groups of HMF and their chemoselectivity. In particular, the carbon atom of the C═O group in HMF has been shown to be the most electrophilic center of the molecule and therefore the most prone to be hydrogenated [25]. In addition, MF tends to further transform into other chemicals via hydrogenation/hydrogenolysis of the C═O bond, ring-opening of the furan ring, and saturation of the furan ring under reductive conditions. Thus, the key to ensure MF formation in high yield is designing an efficient catalytic system that achieves selective hydrogenolysis of the hydroxyl group while preserving the C═O bond and furan ring.

A great deal of effort has been devoted to synthesize MF from HMF. A two-step strategy was developed by adding acid, which involved the conversion of HMF to intermediates such as 5-chloromethylfurfural (CMF), 5-iodomethylfurfural (IMF), or (5-formylfuran-2-yl)methyl formate (FFMF), and then producing MF by hydrogenolysis [19,26,27]. However, this strategy required additional additives (e.g., HCl, HI, or HCOOH), resulting in complexity, poor sustainability, and high cost.

* Corresponding author.
E-mail address: czp@njfu.edu.cn (Z. Chen).

https://doi.org/10.1016/j.apcatb.2023.122893
Received 3 May 2023; Received in revised form 15 May 2023; Accepted 18 May 2023
Available online 19 May 2023

Therefore, it is very attractive to convert HMF to MF via selective hydrogenolysis in a single step. Recently, Han et al. developed a Pt_1/Nb_2O_5 catalyst based on platinum single atoms that could efficiently catalyze the selective hydrogenolysis of HMF to MF [20]. Nevertheless, the preparation of the catalyst and its stability are convoluted.

Herein, we report the first study of the direct selective hydrogenolysis of HMF into MF using gold catalysts supported on anatase (Au/a-TiO_2). In this process, the desired C═O functional group can be preserved and MF can be obtained with a high yield. The performance of the Au/a-TiO_2 catalyst is compared with other supported catalysts, revealing that Au/a-TiO_2 has high activity, excellent stability, and remarkable selectivity to MF. Density functional theory (DFT) simulations and characterization studies indicate that the unusual catalytic performance of Au/a-TiO_2 for the reaction resulted from the weak ability to activate H_2 and adsorb HMF, the selective adsorption of the hydroxy group, the high concentration oxygen vacancies in support, and the appropriately sized Au nanoparticles.

2. Experimental

2.1. Materials

5-Hydroxymethyltetrahydrofurfural (HMF, 99.0 %), 5-methylfurfural (MF, 98.0 %), 2,5-dimethylfuran (DMF, 99.0 %), 2,5-dicarbaldehydefuran (DFF, 98.0 %), 5-methylfurfurylalcohol (MFA, 97.0 %), tetrahydrofuran (99.0 %), n-pentadecane (99.0 %) were purchased from Shanghai Macklin Biochemical Co., Ltd. $HAuCl_4$, $RuCl_3{\cdot}3H_2O$, Pd$(NO_3)_2$, Ni$(NO_3)_2{\cdot}6H_2O$, a-TiO_2 (anatase), r-TiO_2 (rutile), and P25-TiO_2 were purchased from Shanghai Aladdin Bio-Chem Technology Co., Ltd. Al_2O_3 and SiO_2 were provided by the BASF chemical company. All chemicals were used as received without further purification. In addition, the Nb_2O_5 was synthesized according to our previous report [28]. Typically, 19.20 g of self-prepared niobium oxalate solution (Nb: 0.5 mol L^{-1}) and 0.71 g of ammonium oxalate were dissolved in 50 mL of deionized water and sealed in a 100 mL Teflon-lined autoclave, and treated at 180 ℃ for 24 h. The resulting powders were collected and calcined at 400 ℃ for 4 h under air with a heating ramp of 10 ℃ min^{-1}.

2.2. Catalyst preparation

The 2 wt % Au/a-TiO_2 catalysts were prepared by the incipient wetness impregnation. Typically, 0.04 g of $HAuCl_4{\bullet}3H_2O$ was dissolved in 0.5 mL of deionized water. Next, 1 g of a-TiO_2 was added to the aqueous solution of $HAuCl_4$ and mixed thoroughly. The obtained sample was dried at 100 ℃ for 12 h and then calcined in air at 400 ℃ for 4 h with a heating rate of 3 ℃ min^{-1}. In addition, other supports (r-TiO_2, P25-TiO_2, Nb_2O_5, Al_2O_3, and SiO_2) loaded Au catalysts were prepared using the same procedure. The hydrothermal reaction was carried out at 180 ℃ for 1 day. The obtained solid was filtered, washed thoroughly with deionized water, and dried at 80 ℃ overnight. The samples were calcined at 400 ℃ for 4 h. The 2 wt % Ru/TiO_2, 2 wt % Pd/TiO_2, and 2 wt % Ni/TiO_2 catalysts were prepared by incipient wetness impregnation, in which the metal precursors were $RuCl_3$, Pd$(NO_3)_2$, and Ni$(NO_3)_2$, respectively. The obtained sample was dried at 100 ℃ for 12 h and then calcined at 500 ℃ for 3 h, followed by reduction treatment in a 10 vol % H_2/Ar flow at 400 ℃ for 4 h. The metal loading in each catalyst was at ~2 wt %, confirmed by inductively coupled plasma atomic emission spectrometry (ICP-AES).

2.3. Catalyst characterization

Powder X-ray diffraction (XRD) patterns were recorded on a Rigaku D/max-2550VB/PC using Cu Kα radiation ($\lambda = 1.5406$ Å). The catalysts were ground into fine powder before the measurements. Each sample was scanned from $2\theta = 10$–$80°$. Nitrogen adsorption experiments were performed at 77 K on a Micromeritics ASAP 2020 M sorption analyzer. The surface area was calculated by the Brunauer-Emmett-Teller (BET) method, the pore size distribution was calculated by the Barrett-Joyner-Halenda (BJH) method through the desorption branch of the isotherm, and the total pore volume was estimated at a relative pressure of 0.975. Chemical analysis of the samples was performed by using inductively coupled plasma atomic emission spectrometry (Agilent 725ES ICP-AES). Transmission electron microscopy (TEM), high-resolution transmission electron microscope (HRTEM), and energy dispersive spectroscopy (EDS) mappings were examined by using a JEOL JEM-2100EX microscope, and the electron beam accelerating voltage was 200 kV. X-ray photoelectron spectroscopy (XPS) spectra were recorded on a Thermo Scientific Escalab 250 Xi spectrometer equipped with monochromatic Al Kα radiation, and all results were calibrated using the C 1 s peak at 284.8 eV. The electron paramagnetic resonance (EPR) spectra were collected on a Bruker A300 spectrometer at 77 K. *In situ* diffuse reflectance infrared Fourier Transform spectra (DRIFTS) were recorded on a Nicolet NEXUS 670 FT-IR spectrometer equipped with a reaction chamber and a liquid N_2-cooled high-sensitivity mercury cadmium telluride detector. Prior to the FT-IR studies, about 30 mg of the Au/a-TiO_2 was finely ground and placed in the chamber. Before adsorption, the catalyst was activated in flowing He at 300 ℃ for 1.0 h, and then decreased to 30 ℃ to collect the background spectra. For the adsorption of HMF, it was fed into the chamber by flowing HMF vapor in N_2 and the spectra were recorded at 0, 5, and 60 min. Afterward, the chamber was flushed with N_2 at 100, 200, and 300 ℃, respectively, and the spectra were recorded at each temperature. The spectra were recorded with a resolution of 4 cm^{-1} and an accumulation of 64 scans. All spectra were used after subtracting the background.

2.4. Catalytic tests and product analysis

The hydrogenolysis of HMF was carried out in a Teflon-lined stainless-steel autoclave (50 mL). Typically, HMF (0.2 g) and the catalyst (0.1 g) were mixed with tetrahydrofuran (10 mL) in the autoclave. Then, the autoclave was purged with H_2 three times to remove air and pressurized to 5.0 MPa. The autoclave was heated to 230 ℃ under magnetic stirring at 800 rpm and kept for 8 h. After the reaction, the reactor was quenched in an ice-water bath immediately and the liquid phase was separated from the solid catalyst by centrifugation.

The hydrogenolysis of HMF was also tested in a continuous-flow fixed-bed reactor. Typically, 0.5 g of catalyst was packed into the middle portion of the stainless-steel tubular reactor. Then, a feed of HMF in tetrahydrofuran solution (0.08 M) was injected into the reactor by an HPLC pump, which resulted in a weight-hourly space velocity (WHSV) of 0.24 h^{-1}. The hydrogenolysis of HMF was conducted at 160 ℃ and 6.0 MPa H_2 with the H_2 flow rate of 50 mL min^{-1}. The liquid phase was separated from the gas phase and collected by a gas-liquid separator.

The liquid phase was qualitatively analyzed by GC-MS (Shimadzu QP2020 NX) and quantitatively analyzed by GC-FID (Agilent 7890B) with an HP-5 column (30 m × 250 μm). The column temperature began at 50 ℃ (held for 5 min) and was then raised at 10 ℃ min^{-1} to 280 ℃ (held for 2 min). Pentadecane was used as an internal standard for the quantification of liquid products.

2.5. Theoretical simulations

Density functional theory (DFT) simulations were carried out with the Vienna ab initio simulation package (VASP) [29,30]. We used the Perdew-Burke-Ernzerhof (PBE) [31] density functional complemented by Grimme's D3 approach [32] to account for van der Waals interactions. We employed the Hubbard correction [33] with $U_{eff} = 4.2$ eV [34] by means of Dudarev's approach [35] to mitigate electron self-interaction error [36] for the *d* electrons of Ti. Inner electrons were represented by projector augmented-wave (PAW) core potentials [37] while valence electrons were described with plane-waves with a kinetic cut-off energy of 500 eV. A Γ-centered mesh with a reciprocal grid size

narrower than 0.034 $Å^{-1}$ and generated through the Monkhorst-Pack method [38] was used to sample the Brillouin zone. Spin polarization was included when needed.

Bulk lattice parameters for the two polymorphs of TiO_2 (anatase and rutile) and the three metals (Au, Ru, and Ni) were optimized with a kinetic energy cut-off of 700 eV. Au and Ni belong to the Fm-3 m space group, while a-TiO_2, r-TiO_2, and Ru belong to $I4_1$/amd, $P4_2$/mnm, and P63/mmc, respectively. The calculated lattice parameters are in line with the experiments (Table S1). a-TiO_2(101), r-TiO_2(110), Au(111), Ni (111), and Ru(0001) surfaces, which are the most stable terminations of each system, were modeled with periodic boundary conditions. We applied a dipole correction [39] along the z axes and a vacuum region of 15 Å between slabs. a-TiO_2(101) was represented with a $p(1 \times 3)$ slab with 4 layers (24 at. layers), r-TiO_2(110) was described by a $p(4 \times 2)$ slab with 5 layers (15 at. layers), Ru(0001) was represented as a $p(4 \times 4)$ slab with 4 layers, also $p(4 \times 4)$ slabs with 4 layers were employed for Au(111) and Ni(111). In all cases, the two outermost layers were allowed to relax, whereas the other layers were kept fixed to mimic bulk positions.

Reaction energy profiles for H_2 splitting, HMF hydrogenolysis to MF, and HMF dehydrogenation to DFF were computed using as thermodynamic sinks the corresponding clean surface, HMF, H_2, and H_2O. The climbing image nudged elastic band (CI-NEB) approach [40] was employed to identify the transition states and their nature was confirmed by analyzing the numerical frequencies computed with a step size of ± 0.015 Å. All structural and computational details for the DFT simulations can be found online in the ioChem-BD repository [41,42] at https://doi.org/10.19061/iochem-bd-1-276.

3. Results and discussion

3.1. Hydrogenolysis of HMF to MF on oxides

Direct HMF conversion to MF is challenging due to the complex reaction pathways of HMF under reductive conditions, including hydrogenolysis, hydrogenation, dehydrogenation, ring-opening of the furan ring, and saturation of the furan ring (Fig. 1) [10]. The reaction pathway from HMF to MF is direct hydrogenolysis of the hydroxyl group. However, the aldehyde group in HMF is proposed to be labile and could be easy to be converted to a hydroxyl group under reduction conditions [13,43,44]. Furthermore, the competition of the other side reactions such as the ring-opening of the furan ring, saturation of the furan ring, and condensation of feedstocks or intermediates makes the selective production of MF from HMF difficult.

Based on the reaction network, the key to the successful transformation of HMF towards MF is the selective removal of the hydroxy group, while preserving the aldehyde group and furan rings. This can be achieved by only activating the OH while keeping the other functional groups far from the surface. But even if this is the case, two routes are possible for the OH group, either adding a H first to the OH group (hydrogenolysis, red arrows in Fig. 1) or removing the H from the OH moiety (dehydrogenation, green arrows in Fig. 1). Metal oxides are amphoteric thus can either add or remove H from a substrate, and some can realize selective hydrogenolysis of hydroxy using hydrogen as the reducing agent. Therefore, metal oxides with different physical properties (acid-base and reducibility) were tested (Fig. 2**a** and Table S2-S3). While no MF was detected over rutile titania (r-TiO_2), anatase titania (a-TiO_2)presented the best catalytic performance with MF yield of 21.7 %

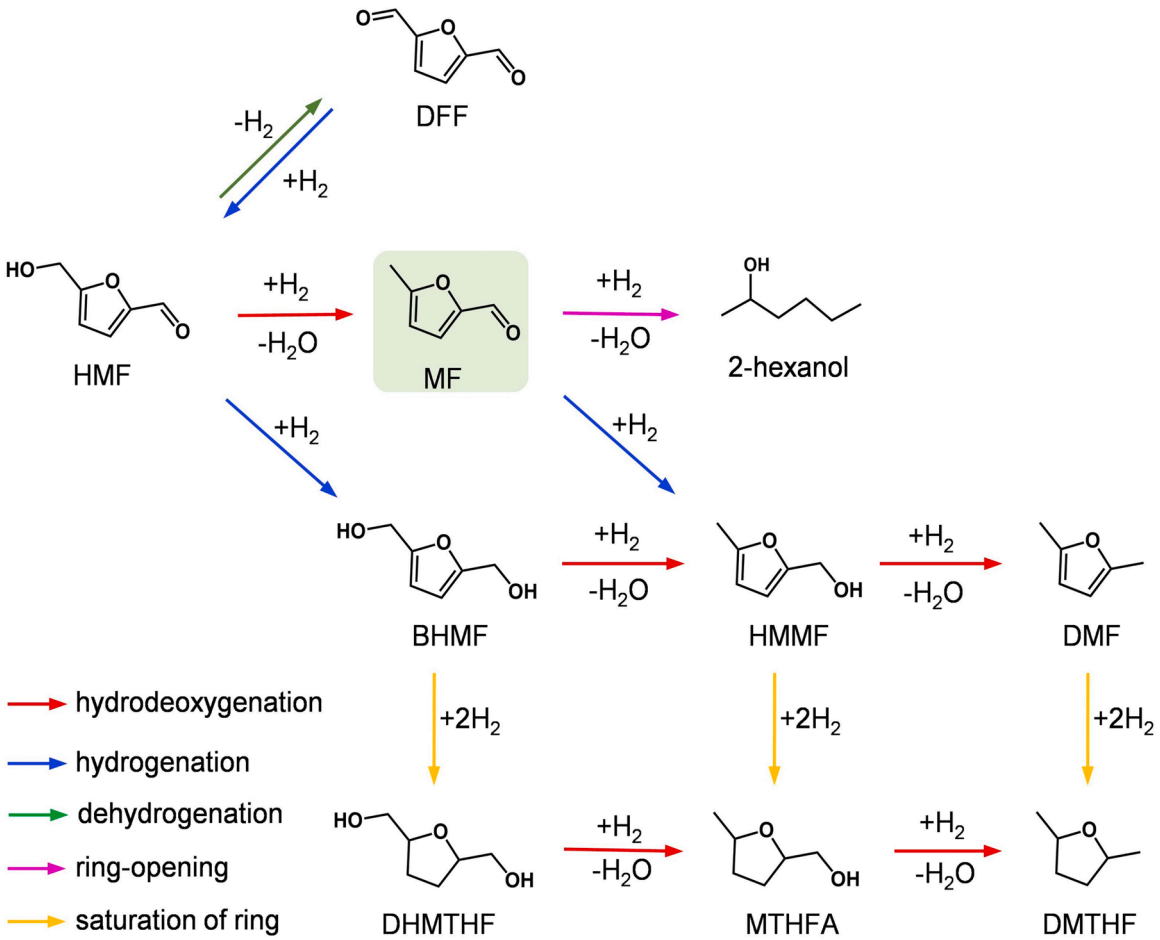

Fig. 1. The reaction pathways and network during the catalytic conversion of HMF under reductive conditions.

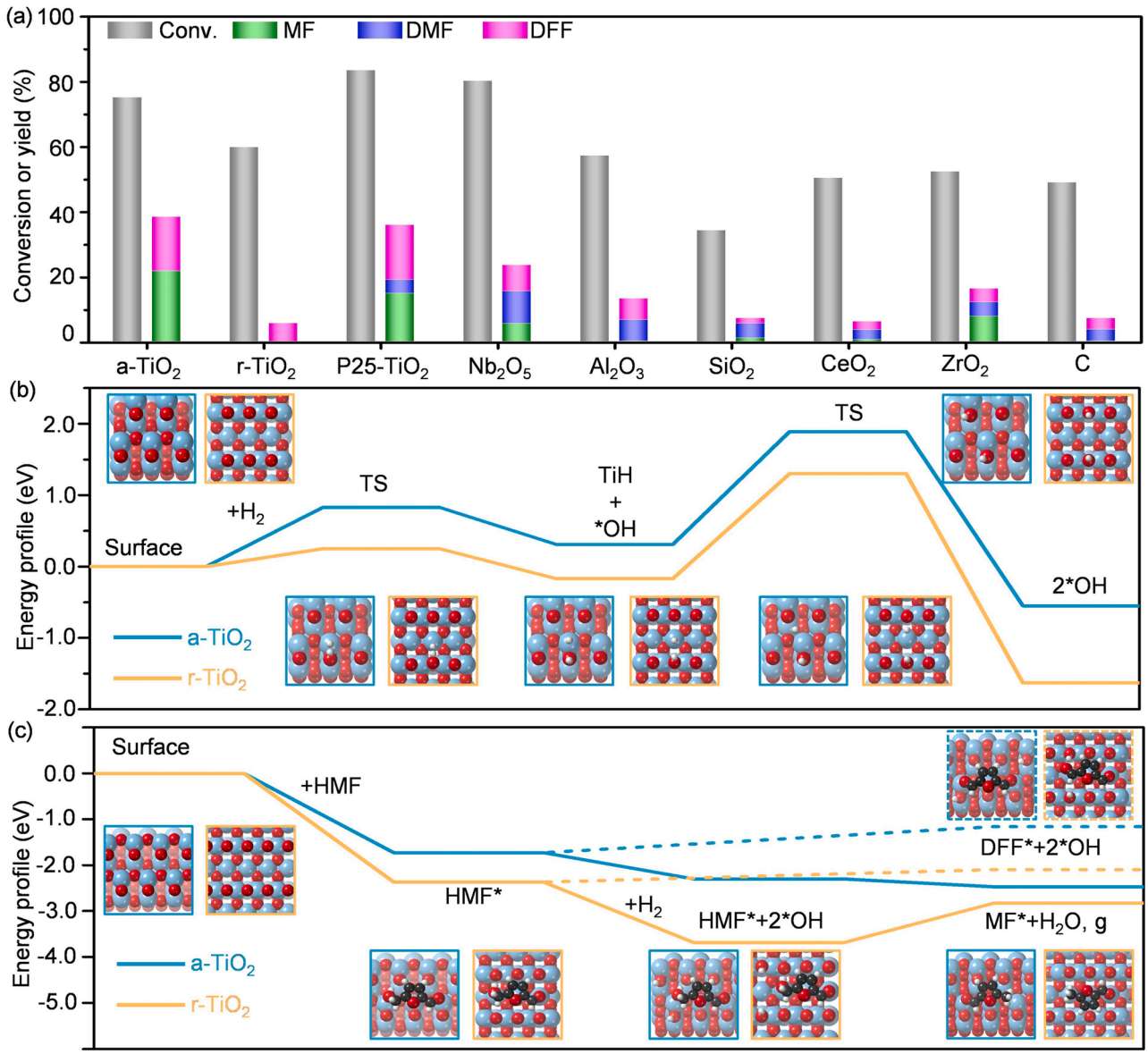

Fig. 2. (a) Summary of results of conversion of HMF over different supports. Reaction conditions: HMF 0.2 g, catalyst 0.1 g, THF 10 mL, H_2 5.0 MPa, 230 ℃ for 8 h. (b) Reaction energy profile for H_2 splitting over a-TiO_2 (101)and r-TiO_2 (110) pristine oxide surfaces. (c) Reaction energy profile of HMF dehydrogenation and hydrogenolysis to DFF and MF, respectively, over pristine a-TiO_2 (101) and r-TiO_2 (110) surfaces. Color code: Ti (light blue), O (red), C (dark gray), and H (white).

and HMF conversion of 75.2 %. Over the P25-TiO_2 (a mixture of 75 % anatase and 25 % rutile), the yield of MF was determined to be 14.9 %, which was slightly lower than a-TiO_2. A high conversion (80.3 %) was obtained over Nb_2O_5, but the yield of MF was only 5.6 % and the major products were 2,5-dimethylfuran (DMF) and 2,5-diformylfuran (DFF). Over CeO_2, the yield of MF was only 0.6 % and the major products were DMF (3.0 %) and DFF (2.6 %). Over ZrO_2, the yield of MF was 7.8 % with 52.3 % conversion of HMF, which was much lower than a-TiO_2. Non-reducible oxides (i.e., Al_2O_3, SiO_2) and activated carbon resulted in very low yields of MF (<1.1 %) and small conversions. However, the carbon balance on a-TiO_2 was only 63.2 % even if no other products were detected in the liquid. This could be explained by the limited hydrogenolysis capacity of a-TiO_2, which led to the undesired condensation of intermediates/products that was catalyzed by acidic or basic sites.

To elucidate the remarkable activity of a-TiO_2 for the conversion of HMF into MF, theoretical investigations using DFT were carried out. We computed the reaction energy profiles for H_2 splitting, and HMF hydrogenolysis to MF and dehydrogenation to DFF over the pristine low-energy surfaces of a-TiO_2(101) and r-TiO_2(110) (Figs. 2**b**, 2**c**, and **S1**). H_2 splitting starts with the heterolytic H_2 dissociation (TiH+*OH), followed by the transfer of the hydride (TiH) to form two hydroxyls (2 *OH) [45]. r-TiO_2 is a better H_2 splitter than a-TiO_2 thus showing a higher surface basicity. From this point, HMF adsorption is easy and its protonation by surface hydroxyls *OH is better on a-TiO_2 than on r-TiO_2. The competing reaction HMF dehydrogenation towards DFF forming surface *OH is favored on r-TiO_2. Thus, from the simulations, the formation of MF is favored on a-TiO_2 while DFF formation is preferential on r-TiO_2. In addition, r-TiO_2 shows very strong adsorption of all HMF-derived intermediates (MF, DFF, DMF, and HMMF) (Fig. S2) and this together with the surface basic properties can catalyze side reactions as condensations. Finally, oxygen vacancies improve HMF adsorption but do not modify the reaction profiles of a-TiO_2 (Fig. S3-S5) while on defective r-TiO_2 HMF adsorption is slightly smaller but favors the MF route.

To further explore the active sites of a-TiO_2, X-ray photoelectron spectroscopy (XPS) was carried out on three TiO_2 supports (i.e., a-TiO_2, r-TiO_2, and P25-TiO_2) to analyze their oxygen species on the surface

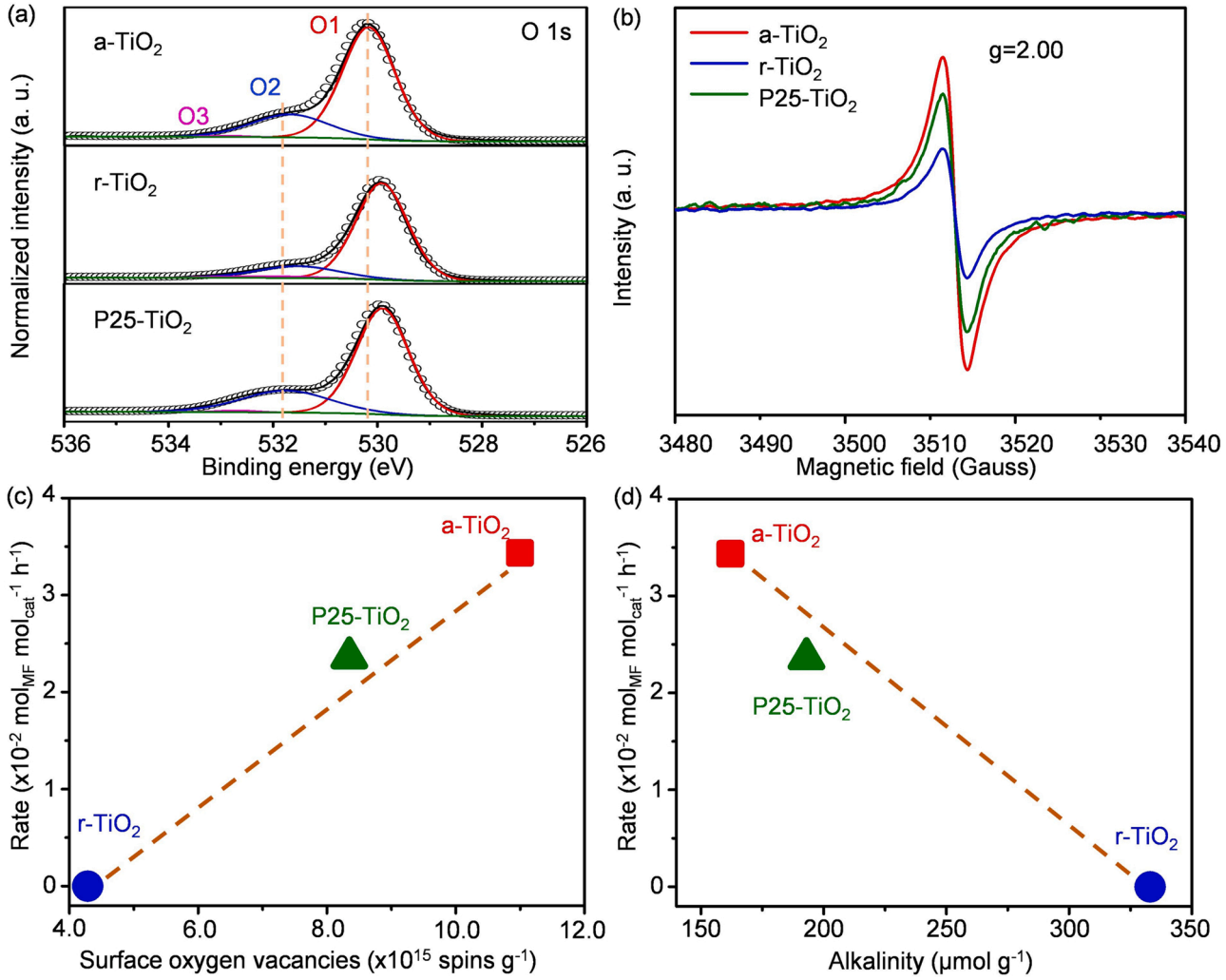

Fig. 3. (a) XPS spectra of O 1s peaks of a-TiO_2, r-TiO_2, and P25-TiO_2 catalysts. O1, O2, and O3 are attributed to lattice oxygen, oxygen vacancies, and dissociated chemisorbed O in metal oxides, respectively. (b) Low-temperature EPR spectra for the a-TiO_2, r-TiO_2, and P25-TiO_2 catalysts. (c) Correlation of the rate of MF formation with the surface oxygen vacancies on catalysts. Based on quantitative EPR analysis, the surface oxygen vacancies on a-TiO_2, r-TiO_2, and P25-TiO_2 catalysts were 10.998×10^{15}, 4.285×10^{15}, and 8.347×10^{15} spins g^{-1}. (d) Correlation of the rate of MF formation with the basic sites on catalysts. Based on quantitative CO_2-TPD analysis (Fig. S6), the basic sites on a-TiO_2, r-TiO_2, and P25-TiO_2 catalysts were 162, 193, and 333 μmol g^{-1}.

(Fig. 3**a**). The O 1 *s* XPS spectra were fitted into three peaks (O1, O2, and O3), which could be attributed to lattice oxygen, oxygen vacancies, and dissociated chemisorbed oxygen in metal oxides, respectively. The ratios of different species of O 1*s* were calculated and summarized in Table S4. Especially, the ratio of oxygen vacancies over a-TiO_2 was up to 28 %, which was higher than that of r-TiO_2 (13 %) and P25-TiO_2 (22 %). Moreover, electronic paramagnetic resonance (EPR) measurements were also employed to explore the oxygen vacancy (Fig. 3**b**). It shows a strong axial signal with a *g* value of 2.003, which is attributed to the single electron $O_2^{\bullet-}$ radical trapped at oxygen vacancies [46,47]. The specific quantification of oxygen vacancies was also given in Table S4, and the density of surface oxygen vacancies decreases in the order of a-TiO_2 > P25-TiO_2 > r-TiO_2, consistent with the order of XPS. As shown in Fig. 3**c**, a positive correlation was identified between the surface oxygen vacancies and the rate of MF formation, i.e., a higher amount of surface oxygen vacancies leads to a higher rate of MF formation.

Our simulations confirm that basic sites usually dominate the dehydrogenation reaction and suppress the hydrogenation reaction. Therefore, the temperature-programmed desorption of carbon dioxide (CO_2-TPD) was carried out to detect the basic site concentration and distribution on the surface of catalysts. As shown in Fig. 3**d** and **S6**, the total basic amount presented in the order that r-TiO_2 > P25-TiO_2 > a-TiO_2, which was a negative coefficient correlated with the catalytic performance. Thus, more oxygen vacancies and fewer and weaker basic sites favor the hydrogenolysis of HMF, consistent with the DFT observations.

3.2. *Metal promotion of the selective hydrogenolysis of HMF to MF on oxides*

3.2.1. *Metal selection*

Metals are known as the active sites for H_2 dissociation to promote the hydrogenolysis reaction and thus they were added to the optimum a-TiO_2 (Fig. 4**a**). Among all the investigated catalysts, Au/a-TiO_2 showed the highest catalytic performance, and the yield of MF was up to 83.1 % with reaching almost full conversion. A few by-products such as DMF and DFF were detected due to the over-hydrogenolysis of MF and dehydrogenation of HMF, respectively. In contrast, Ru/a-TiO_2 can catalyze the further hydrogenation and hydrogenolysis of MF into DMF, due to its high hydrogenation performance. A similar result was obtained for the Pd/a-TiO_2 catalyst, whose major product was DMF (70.4 %). The Pt/a-TiO_2 catalyst showed different product distributions, in which major products were ring-opening of furan ring products, such as 2-hexanol (33.9 %), 1-butanol (10.7 %), 2,5-hexanediol (7.4 %), 2-

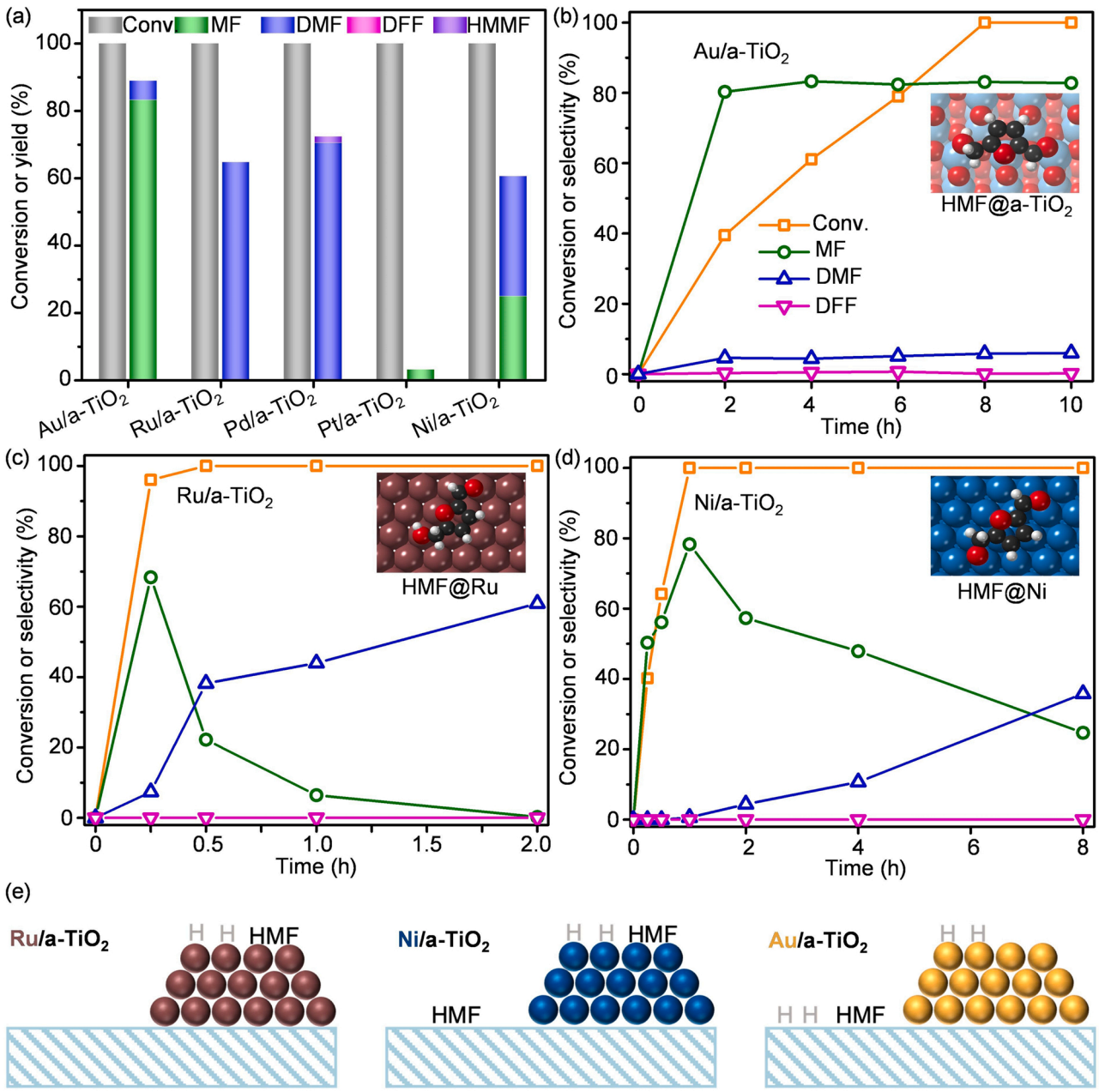

Fig. 4. (a) Summary of results of conversion of HMF over different catalysts. Reaction conditions: HMF 0.2 g, catalyst 0.1 g, THF 10 mL, H_2 5.0 MPa, 230 ℃ for 8 h. (b-d) Product distributions for the conversion of HMF over Au/a-TiO_2, Ru/a-TiO_2, and Ni/a-TiO_2 versus time. Reaction condition: HMF 0.2 g, catalyst 0.1 g, THF 10 mL, H_2 5.0 MPa, 230 °C. (e) Scheme representing the predicted adsorption and activation sites for HMF and H_2 (based on the DFT values shown in Table S5) for Ru/a-TiO_2, Ni/a-TiO_2, and Au/a-TiO_2 catalysts. Color code: hydrogen (gray), HMF (black), TiO_2 (light blue), ruthenium (brown), nickel (blue), and gold (orange).

hexanone (2.8 %), 1-hexanol (1.9 %), and hexane (1.8 %). It was attributed to the fact that metallic Pt (Pt^0) was beneficial for the direct cleavage of the C–O bond in the furan ring [48,49], producing large amounts of ring-opening of furan ring products. Over the Ni/a-TiO_2 catalyst, the yield of MF and DMF were 24.7 % and 35.8 %, respectively. It may be originated from that its hydrogenation activity was lower than that of Ru/a-TiO_2 and Pd/a-TiO_2, but higher than that of Au/a-TiO_2. Furthermore, other metal oxides-supported Au catalysts (Au/r-TiO_2, Au/P25-TiO_2, Au/Nb_2O_5, Au/Al_2O_3, Au/SiO_2, Au/CeO_2, Au/ZrO_2, and Au/C) were also prepared, and their physical properties were summarized in Fig. S7-S14. Over other metal oxides-supported Au catalysts (Fig. S7), the yield of MF and conversion also increased dramatically after loading gold, suggesting that gold species can enhance catalytic performance.

3.2.2. Mechanistic interpretation of the metal/metal oxide synergy

To further explore the reaction pathways and closely monitor the intermediates over different metals, the HMF transformations over Au, Ru, and Ni/a-TiO_2 catalysts were conducted at different times (Fig. 4**b**-4**d**). Although the conversion of HMF increased linearly from 39.5 % to 100 % when increasing the reaction time from 2 to 8 h (Au/a-TiO_2, Fig. 4**b**), the selectivity of MF remained constant between 80.3 % and 83.1 %. The selectivity of MF was not changed despite further prolonging the reaction time to 10 h, confirming the high MF production against the competitive parallel reactions over Au/a-TiO_2. In contrast, the Ru/a-TiO_2 catalyst showed significant differences in product distributions versus time (Fig. 4**c**). The conversion of HMF reached 95 % in 15 minutes with the main product of MF (selectivity = 68.4 %) together with a small amount of DMF (selectivity = 7.4 %), suggesting that the

hydrogenolysis of a hydroxy group was a fast process. On prolonging the reaction time, MF was converted into DMF, indicating the hydrogenation/hydrogenolysis of the aldehyde group in MF. Similar behavior was observed over the Ni/a-TiO_2 despite the lower reaction rate compared to Ru/a-TiO_2 (Fig. 4**d**). Thus, the reaction pathways of the three catalysts were summarized in Fig. S15. Over Au/a-TiO_2, the conversion of HMF was directly converted into MF by the selective hydrogenolysis of the hydroxy group. While over Ru/a-TiO_2 and Ni/a-TiO_2, HMF was first converted into MF by the hydrogenolysis of the hydroxy group, which was followed by further hydrogenation/hydrogenolysis of the aldehyde group into DMF.

To further verify the selective hydrogenolysis of the hydroxy group over different metals, the conversion of various feedstocks was conducted over Au/a-TiO_2 and Ru/a-TiO_2 (Fig. S16). For Au/a-TiO_2, no product was detected in the conversion of MF and DFF, indicating that Au/a-TiO_2 has a poor activity to remove the aldehyde group. Interestingly, 5-methyl-2-furanmethanol (HMMF) with a yield of 52.6 % was produced from 2,5-furandimethanol (BHMF), confirming that Au/a-TiO_2 is active for hydrogenolysis of the hydroxy group. In contrast, high yields of DMF were achieved over Ru/a-TiO_2 in the conversion of MF (66.7 %), DFF (51.0 %), and BHMF (55.5 %), demonstrating the unique performance of Au/a-TiO_2 for the selective hydrogenolysis of the hydroxy group. These results suggested that the Au/a-TiO_2 catalyst showed excellent catalytic activity for the hydrogenolysis of the hydroxy group but low activity for the hydrogenation/hydrogenolysis of the aldehyde group, leading to high MF selectivity.

DFT simulations were carried out to elucidate the factors ruling the catalytic activity and selectivity in Au, Ru, and Ni/a-TiO_2 systems. E_{ads} for the reagents (HMF and H_2), as well as the activation energy for H_2 splitting ($E_{a,H2}$), were computed on Au(111), Ru(0001), and Ni(111) and compared to the values obtained from a-TiO_2 support (Table S5). With these values at hand, we were able to predict if the adsorption of HMF and activation of H_2 takes place on the metal nanoparticles or on the metal oxide support, which is paramount to explain the selectivity of the catalysts (Fig. 4**e**). Ru and Ni clearly enhance H_2 splitting (barrierless) compared to the support (that shows a barrier of 0.83 eV), which allows increasing the conversion but is detrimental to the selectivity. The high amount of available activated H_2 leads to the over-hydrogenation of HMF yielding to DMF. HMF adsorbed better on Ru nanoparticles (E_{ads} = −3.08 eV) than on the oxide, but was competitively adsorbed on Ni and a-TiO_2 support. Therefore, the smaller tendency of Ni to adsorb HMF than Ru allows Ni/a-TiO_2 catalyst to present a higher selectivity to MF than Ru/a-TiO_2. In contrast, H_2 adsorption (E_{ads} = 0.28 eV) shows an activation energy of 0.89 eV on Au which are close to the a-TiO_2 support (E_{ads} = 0.31 eV and E_a = 0.83 eV, respectively). Moreover, the adsorption of HMF is favored on the support over Au nanoparticles. Additionally, the E_{ads} of relevant products (DMF, DFF, MF, and HMMF) on the three metal surfaces confirm that the adsorption is favored in Ru over Ni and it is particularly poor over Au (Fig. S17). Therefore, although Au shows the worst ability to activate H_2 and adsorb HMF, it is the best catalyst for HMF conversion to MF, suggesting the importance of low coverage of active species for high selectivity of MF formation from HMF.

3.2.3. *Au particle size effects on the promotion*

To study the influence of gold particle size, a series of Au/a-TiO_2

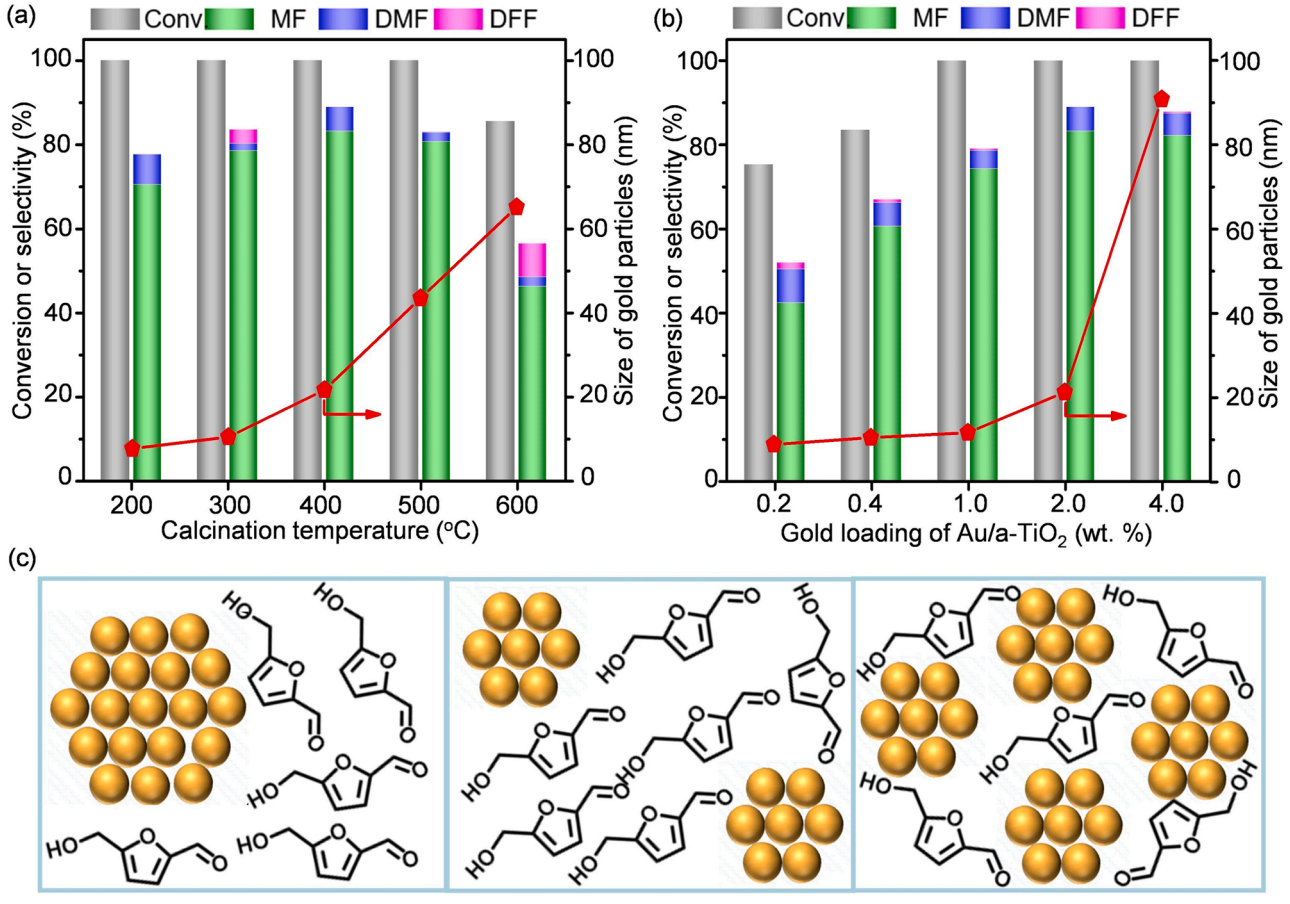

Fig. 5. (a) The effect of the temperature of calcination (200–600 ℃) of Au/a-TiO_2 upon the catalytic performance of the hydrogenolysis of HMF. Reaction conditions: HMF 0.2 g, catalyst 0.1 g, THF 10 mL, H_2 5.0 MPa, 230 ℃ for 8 h. (b) The effect of Au loading of Au/a-TiO_2 upon the catalytic performance of the hydrogenolysis of HMF. Reaction conditions: HMF 0.2 g, catalyst 0.1 g, THF 10 mL, H_2 5.0 MPa, 230 ℃ for 8 h. (c) Schemes showing how the size and distribution of Au nanoparticles can enhance or prevent the interaction and reactivity between HMF molecules.

catalysts with various gold particle sizes were prepared by changing the temperature of calcination or gold content. The average gold particle size was calculated via the Debye-Scherrer equation (Fig. S18). As shown in Fig. 5**a**, the size of gold nanoparticles increases from 7.3 to 64.9 nm when increasing the calcination temperature from 200 to 600 ℃. Although the conversion of HMF remains 100 % when the calcination temperature is below 500 ℃, the selectivity of MF formation first increased and reached a maximum (83.1 %) at 400 ℃ (particle size = 21.3 nm). Further increasing the calcination temperature to 600 ℃ was found detrimental, which decreased the conversion of HMF and selectivity of MF to 85.5 % and 46.1 %, respectively. A similar phenomenon was also observed by varying the loading of gold. The size of Au nanoparticles increases from 8.9 to 90.8 nm with increasing the gold loading from 0.2 to 4.0 wt % (Fig. 5**b**). The conversion of HMF increases when increasing the loading of Au and reaches a plateau of 100 % at the loading of 1.0 wt %. Meanwhile, the selectivity of MF increases from 42.2 % (0.2 wt %) to 83.1 % (2.0 wt %), and further increasing the loading to 4.0 wt % is not beneficial to MF formation. These results suggested that the gold nanoparticle with appropriate diameters (about 20 nm) favors the selective hydrogenolysis of HMF into MF. Therefore, an ideal size and dispersion of the Au nanoparticles allow the generation of spatially resolved sites on the support preventing the interaction between HMF molecules and avoiding the side reactions of condensation, which promotes the selective production of MF from HMF (Fig. 5**c**).

3.3. *In situ* FTIR and stability test of Au/a-TiO_2

In situ Fourier transform infrared spectroscopy (FTIR) was performed to trace the adsorption and transformation of HMF over Au/a-TiO_2. As shown in Fig. 6**a**, the liquid HMF presents characteristic bands at 1190, 1521, 1668, 2824, and 3000–3600 cm^{-1} assigning to the stretching of C–O–C, C═C, C═O, CH_2, and –OH groups. In comparison, the intensities of the bands of C–O–C, C═C, and CH_2 significantly decrease in the case of HMF adsorbed Au/a-TiO_2, indicating that the HMF molecules were disorderly absorbed on the surface of Au/a-TiO_2 with hindered motions. Meanwhile, the stretching mode of -OH shifts to a lower wavenumber (red-shift) on HMF adsorbed Au/a-TiO_2, suggesting that the adsorption of HMF was primarily via its hydroxy group. Interestingly, the stretching mode of C═O (1668 cm^{-1}) is not observably changed upon adsorption, indicating that the adsorption of the aldehyde group is not favorable on the catalyst surface. Furthermore, the desorption of HMF was further conducted and the FTIR spectra at

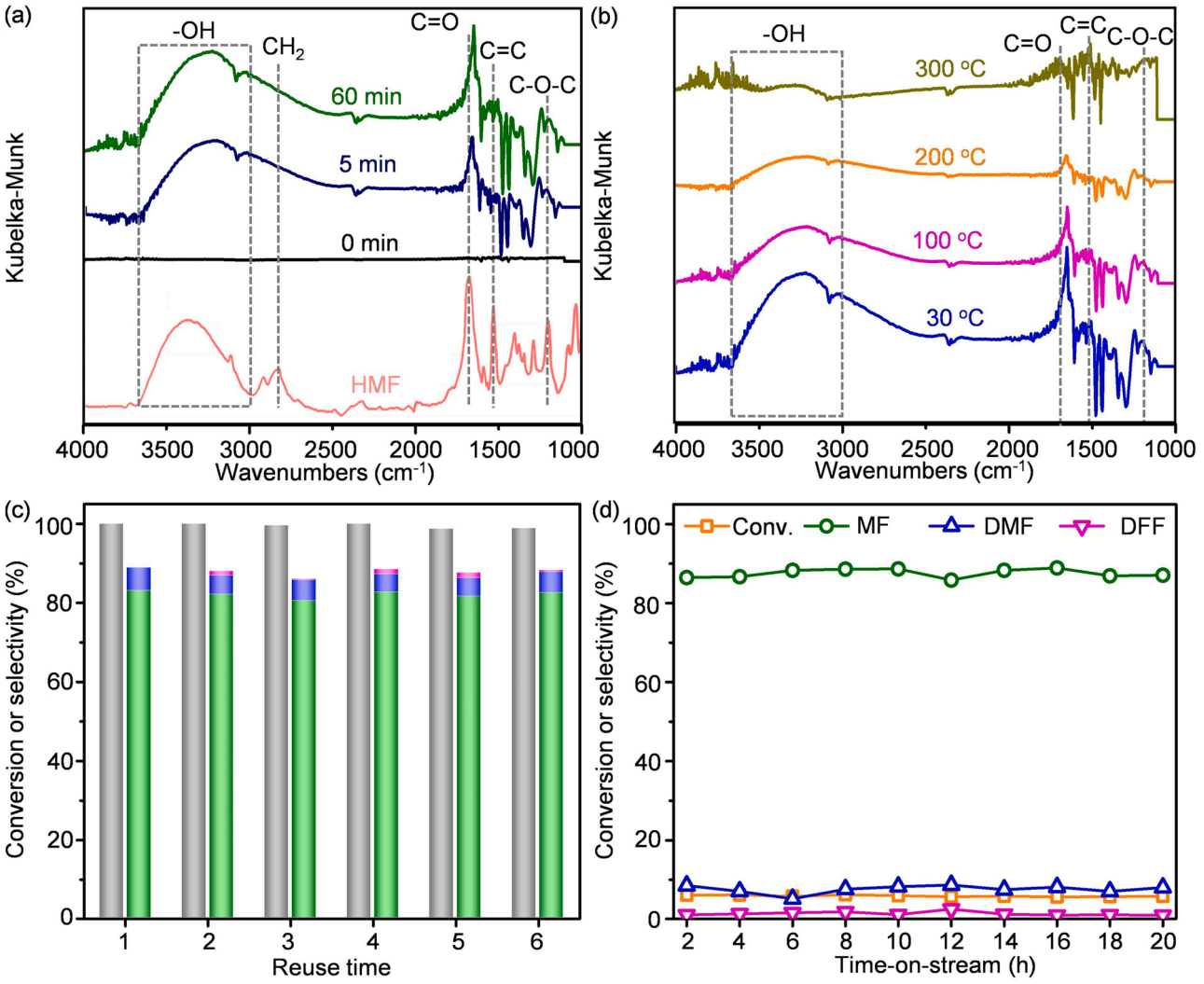

Fig. 6. (a) *In situ* FTIR spectra for Au/a-TiO_2 on adsorption of HMF and the FTIR spectra for solid HMF. The bands at 1190, 1521, 1668, 2824, and 3000–3600 cm^{-1} are assigned to the intensity of C–O–C, C═C, C═O, CH_2, and –OH stretching mode. (b) *In situ* FTIR spectra for Au/a-TiO_2 on desorption of HMF at different temperatures. (c) Performance of Au/a-TiO_2 in five consecutive tests with reuse of the catalysts. Reaction conditions: HMF 0.2 g, 2 %Au/a-TiO_2 0.1 g, THF 10 mL, H_2 5.0 MPa, 230 ℃ for 8 h. (d) Product distribution in the hydrogenolysis of HMF in a fixed-bed reactor over Au/a-TiO_2 catalyst. Reaction conditions: Au/a-TiO_2 0.5 g, HMF 0.08 M, 0.2 mL min^{-1} liquid flow rate, 160 ℃, H_2 6.0 MPa.

different temperatures are shown in Fig. 6**b**. With the increase in the desorption temperature, the intensity of –OH stretching mode at 3000–3600 cm^{-1} and C═O stretching mode at 1668 cm^{-1} decreased gradually, but were still detected at 200 ℃, suggesting that HMF is strongly absorbed on Au/a-TiO_2.

The stability of the resulting Au/a-TiO_2 catalyst was evaluated both in batch and flow operation, which demonstrated robust performance in six consecutive recycling runs (Fig. 6**c**) and 20 h of operation (Fig. 6**d**) without obvious deactivation. Analysis of the used catalyst by XRD, TEM, BET, and ICP, confirms the preservation of the physiochemical properties (Fig. S19, S20, and Table S2).

4. Conclusions

In summary, we develop an efficient gold catalyst on anatase-type titania (Au/a-TiO_2) that can selectively hydrodeoxygenate the hydroxyl group and preserve the aldehyde group, thus affording an exceptional performance for the transformation of HMF to MF with a high-yield of 83.1 % and robust stability both in batch and flow operation. Coupled experimental results and DFT simulations attribute the superior performance of the developed Au/a-TiO_2 catalyst to the following reasons: (1) the different adsorption of HMF on gold and anatase is mandatory to observe high selective hydrogenolysis of the hydroxy group; (2) medium HMF concentrations will lead to polymerization on anatase but both the presence of oxygen vacancies in the support and gold prevent this path by controlling the HMF coverage and molecular orientation on the surface via the selective adsorption of hydroxy group, and (3) the low coverage of active H atoms that can be generated both at the Au nanoparticles or on the metal oxide ensure that the kinetics can be stopped at the desired compound, viz. MF. This study paves the way for the design and preparation of new bifunctional catalysts toward selective hydrogenolysis of biomass to produce chemicals with high value.

CRediT authorship contribution statement

Lin Dong: Methodology, Investigation, Data curation, Formal analysis, Writing - Original Draft. **Jordi Morales-Vidal:** DFT calculations, Formal analysis. **Lili Mu:** *In situ* FTIR, spectrum analysis. **Licheng Li:** *In situ* FTIR, spectrum analysis. **Núria López:** Designed and guided the study, provided insights into DFT calculations; Writing - Review & Editing. **Javier** Pérez-Ramírez Overall direction of the project, guided the experimental and theoretical work; Writing - Review & Editing. **Zupeng Chen:** Conceptualization, Project administration, Writing - Review & Editing, Supervision, Funding acquisition. All the authors discussed the results and co-wrote the manuscript.

Declaration of Competing Interest

The authors declare that they have no known competing financial interests or personal relationships that could have appeared to influence the work reported in this paper.

Data availability

Data will be made available on request.

Acknowledgments

This project was supported financially by the National Natural Science Foundation of China (No. 22002043, 22202105), the Natural Science Foundation of Jiangsu Province (BK20210608), and the Natural Science Foundation of Jiangsu Higher Education Institutions of China (21KJA150003). The Spanish Ministry of Science and Innovation is acknowledged for financial support (PRE2019-088791, PID2021-122516OB-I00, and Severo Ochoa Grant MCIN/AEI/10.13039/501100011033 CEX2019-000925-S) and the Barcelona Supercomputing Center-MareNostrum (BSC-RES) for providing generous computer resources.

Appendix A. Supporting information

Supplementary data associated with this article can be found in the online version at doi:10.1016/j.apcatb.2023.122893.

References

[1] Z. Zhang, J. Song, B. Han, Catalytic transformation of lignocellulose into chemicals and fuel products in ionic liquids, Chem. Rev. 117 (2017) 6834–6880.
[2] Z.H. Sun, B. Fridrich, A. de Santi, S. Elangovan, K. Barta, Bright side of lignin depolymerization: toward new platform chemicals, Chem. Rev. 118 (2018) 614–678.
[3] Y. Jing, Y. Guo, Q. Xia, X. Liu, Y. Wang, Catalytic production of value-added chemicals and liquid fuels from lignocellulosic biomass, Chem 5 (2019) 2520–2546.
[4] C. Mondelli, G. Gozaydin, N. Yan, J. Pérez-Ramírez, Biomass valorisation over metal-based solid catalysts from nanoparticles to single atoms, Chem. Soc. Rev. 49 (2020) 3764–3782.
[5] Y. Roman-Leshkov, C.J. Barrett, Z.Y. Liu, J.A. Dumesic, Production of dimethylfuran for liquid fuels from biomass-derived carbohydrates, Nature 447 (2007) 982–985.
[6] H.B. Zhao, J.E. Holladay, H. Brown, Z.C. Zhang, Metal chlorides in ionic liquid solvents convert sugars to 5-hydroxymethylfurfural, Science 316 (2007) 1597–1600.
[7] R.J. van Putten, J.C. van der Waal, E. de Jong, C.B. Rasrendra, H.J. Heeres, J.G. de Vries, Hydroxymethylfurfural, a versatile platform chemical made from renewable resources, Chem. Rev. 113 (2013) 1499–1597.
[8] M. Besson, P. Gallezot, C. Pinel, Conversion of biomass into chemicals over metal catalysts, Chem. Rev. 114 (2014) 1827–1870.
[9] F. Chacon-Huete, C. Messina, B. Cigana, P. Forgione, Diverse applications of biomass-derived 5-hydroxymethylfurfural and derivatives as renewable starting materials, ChemSusChem 15 (2022), e202200328.
[10] S. Chen, R. Wojcieszak, F. Dumeignil, E. Marceau, S. Royer, How catalysts and experimental conditions determine the selective hydroconversion of furfural and 5-hydroxymethylfurfural, Chem. Rev. 118 (2018) 11023–11117.
[11] P. Maki-Arvela, D. Ruiz, D.Y. Murzin, Catalytic hydrogenation/hydrogenolysis of 5-hydroxymethylfurfural to 2,5-dimethylfuran, ChemSusChem 14 (2021) 150–168.
[12] X. Qi, H. Guo, L. Li, R.L. Smith Jr., Acid-catalyzed dehydration of fructose into 5-hydroxymethylfurfural by cellulose-derived amorphous carbon, Biomass Convers. Biorefinery 5 (2012) 2215–2220.
[13] S. Xiang, L. Dong, Z.-Q. Wang, X. Han, L.L. Daemen, J. Li, Y. Cheng, Y. Guo, X. Liu, Y. Hu, A.J. Ramirez-Cuesta, S. Yang, X.-Q. Gong, Y. Wang, A unique Co@CoO catalyst for hydrogenolysis of biomass-derived 5-hydroxymethylfurfural to 2,5-dimethylfuran, Nat. Commun. 13 (2022) 3657.
[14] T. Thananatthanachon, T.B. Rauchfuss, Efficient production of the liquid fuel 2,5-dimethylfuran from fructose using formic acid as a reagent, Angew. Chem. Int. Ed. 49 (2010) 6616–6618.
[15] G.H. Wang, J. Hilgert, F.H. Richter, F. Wang, H.J. Bongard, B. Spliethoff, C. Weidenthaler, F. Schuth, Platinum-cobalt bimetallic nanoparticles in hollow carbon nanospheres for hydrogenolysis of 5-hydroxymethylfurfural, Nat. Mater. 13 (2014) 294–301.
[16] L. Xu, R.F. Nie, X.J. Chen, Y.C. Li, Y.X. Jiang, X.Y. Lu, Formic acid enabled selectivity boosting in transfer hydrogenation of 5-hydroxymethylfurfural to 2,5-furandimethanol on highly dispersed Co-N_x sites, Catal. Sci. Technol. 11 (2021) 1451–1457.
[17] R. Alamillo, M. Tucker, M. Chia, Y. Pagán-Torres, J. Dumesic, The selective hydrogenation of biomass-derived 5-hydroxymethylfurfural using heterogeneous catalysts, Green. Chem. 14 (2012) 1413–1419.
[18] X. Hu, Z. Li, H. Wang, H. Xin, S. Li, C. Wang, L. Ma, Q. Liu, Selective hydrogenolysis of 5–hydroxymethylfurfural to 2–hexanol over Au/ZrO_2 catalysts, ChemSusChem (2022), https://doi.org/10.1002/cssc.202200092.
[19] G. Sun, J. An, H. Hu, C. Li, S. Zuo, H. Xia, Green catalytic synthesis of 5-methylfurfural by selective hydrogenolysis of 5-hydroxymethylfurfural over size-controlled Pd nanoparticle catalysts, Catal. Sci. Technol. 9 (2019) 1238–1244.
[20] S. Li, M. Dong, J. Yang, X. Cheng, X. Shen, S. Liu, Z.-Q. Wang, X.-Q. Gong, H. Liu, B. Han, Selective hydrogenation of 5-(hydroxymethyl)furfural to 5-methylfurfural over single atomic metals anchored on Nb_2O_5, Nat. Commun. 12 (2021) 584.
[21] K. Michail, V. Matzi, A. Maier, R. Herwig, J. Greilberger, H. Juan, O. Kunert, R. Wintersteiger, Hydroxymethylfurfural: an enemy or a friendly xenobiotic? A bioanalytical approach, Anal. Bioanal. Chem. 387 (2007) 2801–2814.
[22] M.E. Jung, G.Y. Im, Total synthesis of racemic laurenditerpenol, an HIF-1 inhibitor, J. Org. Chem. 74 (2009) 8739–8753.
[23] K.I. Galkin, V.P. Ananikov, Towards improved biorefinery technologies: 5-methylfurfural as a versatile C_6 platform for biofuels development, ChemSusChem 12 (2019) 185–189.
[24] J. Xu, X. Miao, L. Liu, Y. Wang, W. Yang, Direct synthesis of 5–methylfurfural from D-fructose by iodide-mediated transfer hydrogenation, ChemSusChem 14 (2021) 5311–5319.

[25] R. Goyal, B. Sarkar, A. Bag, N. Siddiqui, D. Dumbre, N. Lucas, S.K. Bhargava, A. Bordoloi, Studies of synergy between metal-support interfaces and selective hydrogenation of HMF to DMF in water, J. Catal. 340 (2016) 248–260.
[26] M.R. Grochowski, W. Yang, A. Sen, Mechanistic study of a one-step catalytic conversion of fructose to 2,5-dimethyltetrahydrofuran, Chem. Eur. J. 18 (2012) 12363–12371.
[27] M. Mascal, E.B. Nikitin, Dramatic advancements in the saccharide to 5-(chloromethyl)furfural conversion reaction, ChemSusChem 2 (2019) 859–861.
[28] Y. Xin, L. Dong, Y. Guo, X. Liu, Y. Hu, Y. Wang, Correlation of the catalytic performance with Nb_2O_5 surface properties in the hydrodeoxygenation of lignin model compound, J. Catal. 375 (2019) 202–212.
[29] G. Kresse, J. Furthmüller, Efficiency of ab-initio total energy calculations for metals and semiconductors using a plane-wave basis set, Comput. Mater. Sci. 6 (1996) 15–50.
[30] G. Kresse, J. Furthmüller, Efficient iterative schemes for ab initio total-energy calculations using a plane-wave basis set, Phys. Rev. B 54 (1996) 11169–11186.
[31] J.P. Perdew, K. Burke, M. Ernzerhof, Generalized gradient approximation made simple, Phys. Rev. Lett. 77 (1996) 3865–3868.
[32] S. Grimme, J. Antony, S. Ehrlich, H. Krieg, A consistent and accurate ab initio parametrization of density functional dispersion correction (DFT-D) for the 94 elements H-Pu, J. Chem. Phys. 132 (2010), 154104.
[33] J. Hubbard, Electron correlations in narrow energy bands, Proc. R. Soc. Lond. Ser. A-Math. Phys. Eng. Sci. 276 (1963) 238–257.
[34] V. Paunović, M. Rellán-Piñeiro, N. López, J. Pérez-Ramírez, Activity differences of rutile and anatase TiO_2 polymorphs in catalytic HBr oxidation, Catal. Today 369 (2021) 221–226.
[35] S.L. Dudarev, G.A. Botton, S.Y. Savrasov, C.J. Humphreys, A.P. Sutton, Electron-energy-loss spectra and the structural stability of nickel oxide: an LSDA+U study, Phys. Rev. B 57 (1998) 1505–1509.
[36] J.L. Bao, L. Gagliardi, D.G. Truhlar, Self-interaction error in density functional theory: an appraisal, J. Phys. Chem. Lett. 9 (2018) 2353–2358.
[37] P.E. Blöchl, Projector augmented-wave method, Phys. Rev. B 50 (1994) 17953–17979.
[38] H.J. Monkhorst, J.D. Pack, Special points for brillouin-zone integrations, Phys. Rev. B 13 (1976) 5188–5192.
[39] G. Makov, M.C. Payne, Periodic boundary conditions in ab initio calculations, Phys. Rev. B 51 (1995) 4014–4022.
[40] G. Henkelman, B.P. Uberuaga, H. Jónsson, A climbing image nudged elastic band method for finding saddle points and minimum energy paths, J. Chem. Phys. 113 (2000) 9901–9904.
[41] M. Álvarez-Moreno, C. De Graaf, N. López, F. Maseras, J.M. Poblet, C. Bo, Managing the computational chemistry big data problem: the ioChem-BD platform, J. Chem. Inf. Model 55 (2015) 95–103.
[42] C. Bo, F. Maseras, N. López, The role of computational results databases in accelerating the discovery of catalysts, Nat. Catal. 1 (2018) 809–810.
[43] Y.H. Zu, P.P. Yang, J.J. Wang, X.H. Liu, J.W. Ren, G.Z. Lu, Y.Q. Wang, Efficient production of the liquid fuel 2,5-dimethylfuran from 5-hydroxymethylfurfural over Ru/Co_3O_4 catalyst, Appl. Catal. B: Environ. 146 (2014) 244–248.
[44] P.P. Yang, Q.N. Xia, X.H. Liu, Y.Q. Wang, Catalytic transfer hydrogenation/hydrogenolysis of 5-hydroxymethylfurfural to 2,5-dimethylfuran over Ni-Co/C catalyst, Fuel 187 (2017) 159–166.
[45] G. Hu, Z. Wu, D.-E. Jiang, First principles insight into H_2 activation and hydride species on TiO_2, Surf. J. Phys. Chem. C 122 (2018) 20323–20328.
[46] N. Liu, M. Xu, Y. Yang, S. Zhang, J. Zhang, W. Wang, L. Zheng, S. Hong, M. Wei, $Au^{\delta-}$-O_v-Ti^{3+} interfacial site: catalytic active center toward low-temperature water gas shift reaction, ACS Catal. 9 (2019) 2707–2717.
[47] S. Wu, X. Tan, J. Lei, H. Chen, L. Wang, J. Zhang, Ga-doped and Pt-loaded porous TiO_2-SiO_2 for photocatalytic nonoxidative coupling of methane, J. Am. Chem. Soc. 141 (2019) 6592–6600.
[48] R. Ma, X. Wu, T. Tong, Z. Shao, Y. Wang, X. Liu, Q. Xia, X. Gong, The critical role of water in the ring opening of furfural alcohol to 1,2-pentanediol, ACS Catal. 7 (2017) 333–337.
[49] T. Tong, X. Liu, Y. Guo, M.N. Banis, Y. Hu, Y. Wang, The critical role of CeO_2 crystal-plane in controlling Pt chemical states on the hydrogenolysis of furfuryl alcohol to 1,2-pentanediol, J. Catal. 365 (2018) 420–428.